









Mature Diffuse Tectonic Block Boundary Revealed by the 2020 Southwestern Puerto Rico Seismic Sequence

U. S. ten Brink¹ , E. A. Vanacore² , E. J. Fielding³ , J. D. Chaytor¹ , A. M. López-Venegas² ,
W. E. Baldwin¹ , D. S. Foster¹ , and B. D. Andrews¹ 

¹U.S. Geological Survey, Woods Hole Science Center, Woods Hole, MA, USA, ²Department of Geology, University of Puerto Rico, Mayaguez, Puerto Rico, ³Jet Propulsion Laboratory, California Institute of Technology, Pasadena, CA, USA

Key Points:

- Seismic activity did not follow the main shock-aftershock sequence and likely ruptured multiple faults in southwest Puerto Rico
- Geologic indicators suggest long-term diffuse deformation due perhaps to heterogeneous arc composition
- This zone may be the southernmost domain of a diffuse deformation boundary between Hispaniola and Puerto Rico

Supporting Information:

Supporting Information may be found in the online version of this article.

Correspondence to:

U. ten Brink,
utenbrink@usgs.gov

Citation:

ten Brink, U. S., Vanacore, E. A., Fielding, E. J., Chaytor, J. D., López-Venegas, A. M., Baldwin, W. E., et al. (2022). Mature diffuse tectonic block boundary revealed by the 2020 southwestern Puerto Rico seismic sequence. *Tectonics*, *41*, e2021TC006896. <https://doi.org/10.1029/2021TC006896>

Received 7 MAY 2021
Accepted 1 FEB 2022

Abstract Distributed faulting typically tends to coalesce into one or a few faults with repeated deformation. The progression of clustered medium-sized ($\geq M_w 4.5$) earthquakes during the 2020 seismic sequence in southwestern Puerto Rico (SWPR), modeling shoreline subsidence from InSAR, and sub-seafloor mapping by high-resolution seismic reflection profiles, suggest that the 2020 SWPR seismic sequence was distributed across several short intersecting strike-slip and normal faults beneath the insular shelf and upper slope of Guayanilla submarine canyon. Multibeam bathymetry map of the seafloor shows significant erosion and retreat of the shelf edge in the area of seismic activity as well as slope-parallel lineaments and submarine canyon meanders that typically develop over geological time. The T -axis of the moderate earthquakes further matches the extension direction previously measured on post early Pliocene ($\sim >3$ Ma) faults. We conclude that although similar deformation has likely taken place in this area during recent geologic time, it does not appear to have coalesced during this time. The deformation may represent the southernmost part of a diffuse boundary, the Western Puerto Rico Deformation Boundary, which accommodates differential movement between the Puerto Rico and Hispaniola arc blocks. This differential movement is possibly driven by the differential seismic coupling along the Puerto Rico—Hispaniola subduction zone. We propose that the compositional heterogeneity across the island arc retards the process of focusing the deformation into a single fault. Given the evidence presented here, we should not expect a single large event in this area but similar diffuse sequences in the future.

1. Introduction

The 2019–2020 seismic swarm in southwestern Puerto Rico (SWPR; Figure 1) consisted of +13,000 earthquakes ($M \geq 2.5$) with 43 earthquakes with $M_w \geq 4.5$ since its start on December 28, 2019. The largest of these events, the $M_w 6.4$ on January 7, 2020 was located offshore and had a mixed normal and strike-slip motion (Liu et al., 2020, ANSS-ComCat). The earthquake sequence and in particular the $M_w 6.4$ earthquake caused extensive damage in coastal towns (Miranda et al., 2020; Morales-Velez et al., 2020; Von Hillebrandt Andrade et al., 2020), co-seismic subsidence around Guayanilla Bay (Allstadt et al., 2020; Fielding et al., 2020; Pérez-Valentín et al., 2021), liquefaction, ground failures, and the collapse of an iconic coastal rock bridge (Allstad et al., 2020; López-Venegas, Vanacore, & Hughes, 2020; López-Venegas, Vanacore, Hughes, Báez-Sánchez, & Hudgins, 2020; Pérez-Valentín et al., 2021). The prolonged seismic activity had thus created anxiety among the island's population. The activity was centered around a defunct oil refinery and strategic facilities for the island, such as a liquid natural gas terminal, and an electric power station.

This seismic activity as expressed in the earthquakes' b -value is not a typical foreshock, main shock, and aftershock sequence (Dascher-Cousineau et al., 2020). Based on the time series of the b -values, Dascher-Cousineau et al. (2020) interpreted this earthquake activity to indicate that the observed seismic activity to date is part of a foreshock sequence with a larger main shock yet to come. An alternative view which we discuss here is that the seismic activity represents the rupture of many faults that are part of a diffuse block boundary within the Greater Antilles island arc. A similar diffuse block boundary and associated sequences of seismic activity had been suggested for the 70–100-km-wide Central Costa Rica Deformed Belt across the Costa Rica volcanic arc, which separates the Middle America subduction zone from the Panama Block (Marshall et al., 2000).

We address the following questions: (a) Can we identify the faults responsible for the 2019–2020 seismic sequence? (b) Is the activity organized in a predictable way? (c) Is it a recurring activity? (4) What framework tectonics generated this activity?

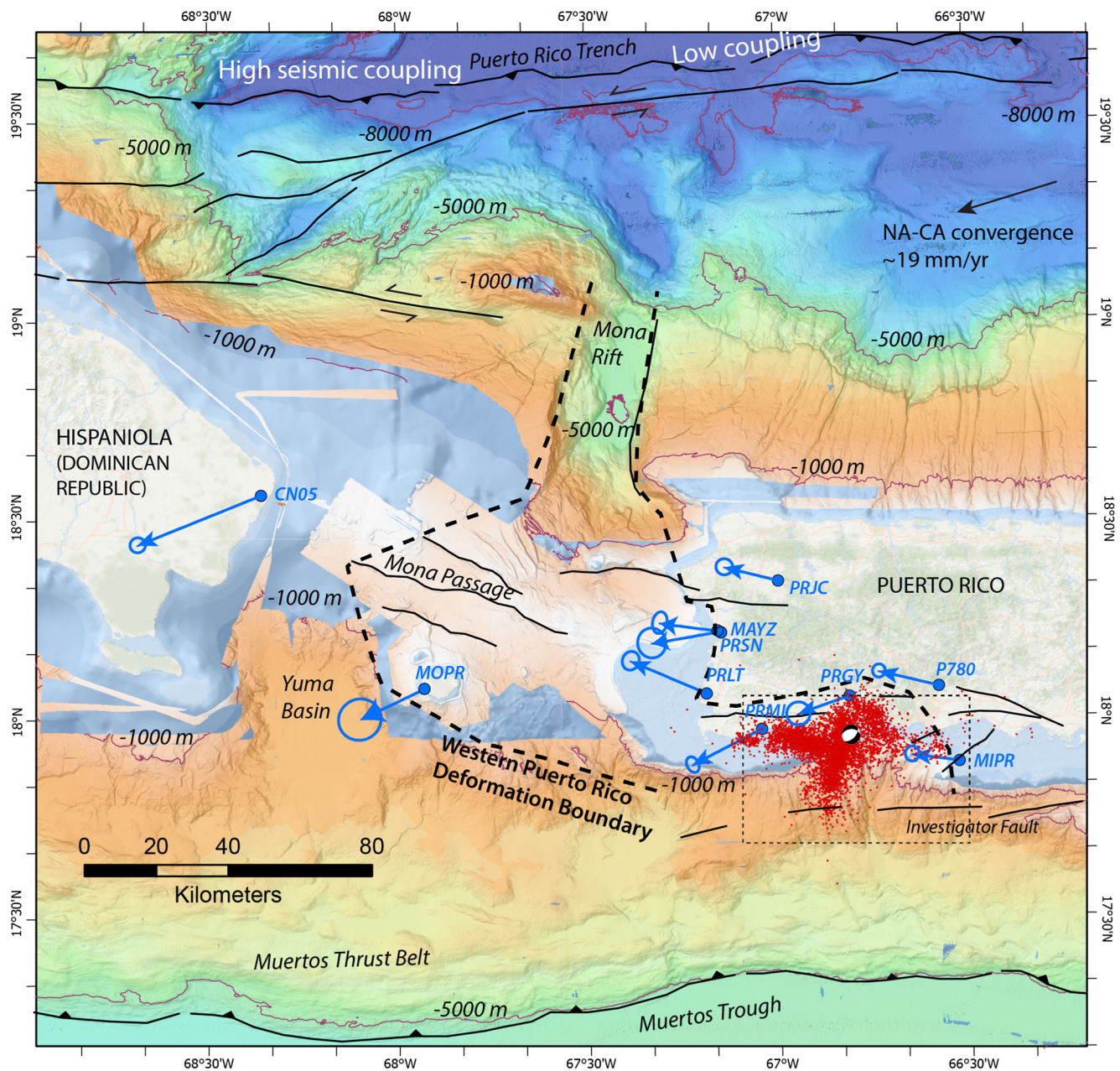


Figure 1. Regional map. Shaded multibeam bathymetry (Andrews et al., 2014) colored by water depth with selected depth contours (thin purple lines). Areas without multibeam bathymetry from GEBCO global bathymetry and are shaded light blue. Red dots – $M \geq 2.5$ earthquakes in the southwestern Puerto Rico seismic sequence from ANSS-ComCat. Beach ball – Epicenter of the largest earthquake during the 2020 seismic sequence, the January 7, 2020 Mw6.4. Black lines – Major faults after Geist and ten Brink (2021). Blue lines – GPS vectors with length proportional to long-term velocities relative to fixed Caribbean plate from the Nevada Geodetic Laboratory (Table S2 in Supporting Information S1). Area between dashed lines is our proposed Western Puerto Rico Deformation Boundary. Dotted black rectangle – Location of Figure 2.

Most of the activity during this sequence occurred offshore. Mapping faults relied on several lines of evidence: (a) Mapping faults in the shallow sub-seafloor by marine high-resolution seismic reflection survey and evaluating seafloor geomorphology; (b) Matching vertical and horizontal displacement models to observed InSAR coastal deformation around the January 7, 2020 Mw6.4 earthquake and the July 3, 2020 Mw5.3 earthquake; (c) Identifying clusters of medium earthquakes and drawing possible faults based on their focal mechanisms.

2. Background

Bedrock in Puerto Rico and Hispaniola formed as part of the inactive Mesozoic and early Cenozoic Greater Antilles island arc that accommodated southwestward subduction of the North American plate under the Caribbean plate. Subduction direction is inferred to have changed to WSW starting ~40 Myr ago (Pindell & Kennan, 2009) resulting in a very oblique convergence along the trench north of Puerto Rico (Figure 1; DeMets et al., 2000). Muertos thrust belt, a wedge of deformed sediment south of the island accommodates thrusting of the arc over the Caribbean plate interior (ten Brink et al., 2009).

The 2020 seismic sequence occurred mostly within the insular shelf and slope south of Puerto Rico (Figure 1). The slope there is dissected by the tributaries of Guayanilla Canyon, which cuts down through unconsolidated Quaternary deposits, the middle Miocene to Early Pliocene shelf carbonates of the Ponce Formation, and the deeper Juan Diaz Formation chalks (Trumbull & Garrison, 1973). The Guayanilla canyon system is the only significant submarine drainage along the south coast of Puerto Rico. The canyon system has eroded into the insular shelf, forming an asymmetric amphitheater (Figures 1 and 2). West and east of this canyon system, the shelf edge is oriented roughly W-E and canyon systems are largely absent. The shelf width is ≤ 12 km west and ≤ 18 km east of the canyon area, respectively, but is as narrow as 1 km in the canyon area, where shallow channels dissect modern reef structures.

A few Holocene and Plio-Pleistocene faults have been mapped onshore in the vicinity of the 2019–2020 SWPR seismic swarm. Mid-Holocene faults were trenched in Lajas Valley (Prentice & Mann, 2005) and near Ponce (Piety et al., 2018; Figure 2). A fault, named San Francisco Fault, was extrapolated from onshore into Guayanilla Bay (Grossman, 1963). A 33-km-long left-lateral strike-slip fault, named Punta Montalva Fault, stretching from Punta Montalva to north Boquerón Bay on the west coast of Puerto Rico was postulated largely based on morphology by Roig-Silva et al. (2013; Figure 3). Garrison (1969) interpreted a several-hundred-millisecond-deep half-graben from Sparker seismic reflection data on the insular shelf south of Ponce. The graben is bounded by the Caja de Muertos Fault on the SE and possibly the Bajo Tasmanian Fault on the NW (Figure 2). Caja De Muertos Island was proposed to have been uplifted by faulting during the Miocene or later (Kaye, 1957). The area of seismic activity is largely devoid of good quality seismic reflection data.

3. Data and Methods

We conducted a high-resolution multichannel seismic survey horizon between March 7 and 13, 2020 aboard the University of Puerto Rico's R/V Sultana based at the Marine Sciences Laboratory at Magueyes Island in La Parguera (Figures 2 and 4). The seismic sources included a 2.4 kJ Sparker at water depths >500 m, a 1 kJ Sparker at water depths of 100–500 m and a 0.3 kJ mini-sparker on the 8–25 m deep shelf. Acoustic data was received by a 32-channel digital streamer with hydrophone group interval of 1.5625 m. Navigation was carried out by a Hemisphere R131 Differential and WAAS (Wide Angle Augmentation System) enabled GPS receiver with horizontal accuracy of 2–3 m (Baldwin et al., 2021). A total of 250-line km were collected with common mid-point (CMP) spacing of 0.781 m for lines on the shelf and 3.125 m for lines on the insular slope. The vertical resolution is estimated to be \pm a few meters. Data processing included geometry definition, trace edits, static correction, noise reduction (f-k deconvolution, f-k filtering, bandpass filtering (70–1,000 Hz), CMP stack, post-stack phase-shift time migration, and spiking deconvolution. Horizon and fault interpretation and visualization were carried out with Kingdom Suite© software. Data penetration was typically ≤ 0.5 s (~ 500 m) on the slope and ≤ 0.08 s on the shelf (Figure 4). Deeper penetration on the shelf was masked by multiples due to the shallow and sometimes hard modern reef bottom.

Multibeam bathymetry data, collected by the NOAA ships Nancy Foster and Thomas Jefferson prior to 2019, and LIDAR data, collected by NOAA on the insular shelf (see Text S1 in Supporting Information S1 for data sources), were gridded at 8 m horizontal resolution. We added these data to an existing compilation of multibeam bathymetry data in the NE Caribbean (Andrews et al., 2014).

Synthetic Aperture Radar interferometry (InSAR) measurements of radar line-of-sight (LOS) combined data from different directions to estimate two components of the surface displacement. InSAR measurements from satellites in this region are sensitive to the east and vertical components. The data included C-band (5.6 cm wavelength) SAR from the Copernicus Sentinel-1 satellites, operated by the European Space Agency (ESA), and

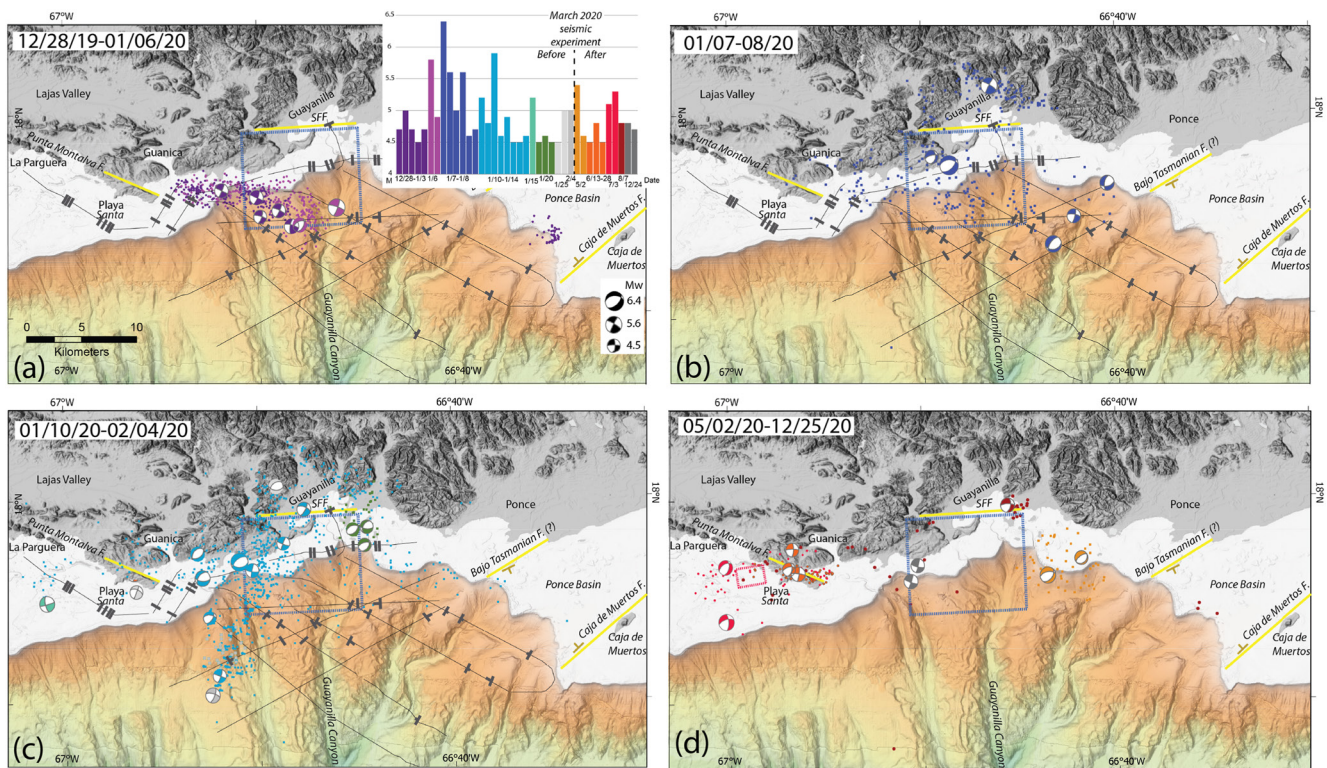


Figure 2. Locations and focal mechanisms of $M_w \geq 4.5$ earthquake clusters (from ANSS-ComCat) colored by date. Inset shows dates of the clusters and color code. Gray earthquakes are moderate earthquakes not associated with a cluster. Some alternate epicenters from the catalog are shown, as discussed in the text and listed in Table S1 in Supporting Information S1. Colored dots – Relocated microseismicity using HypoDD (Vanacore et al., 2021) for a few selected dates, with colors matching the dates of focal mechanisms and the inset. Thin lines – locations of seismic reflection profiles collected between March 7 and 13, 2020, Heavy black marks – Faults interpreted from the seismic reflection profiles with small perpendicular marks denoting apparent dip direction. Dotted rectangles – Modeled fault planes from the Synthetic Aperture Radar interferometry observations (Figures 5 and 6) with colors matching the dates of the focal mechanisms and inset. Yellow lines – published faults. Background – Shaded bathymetry colored by depth (white – 100 m to blue – 2,000 m) and SRTM hill-shaded topography (gray). SFF – San Francisco Fault.

L-band (24 cm wavelength) SAR from the Japan Aerospace Exploration Agency (JAXA) Advanced Land Observation Satellite-2 (ALOS-2) satellite. Two tracks of Sentinel-1 data cover the land area of the seismic activity, and another track covers the area to the east. SAR and InSAR processing were done with the InSAR Scientific Computing Environment (ISCE) v2 (Rosen et al., 2012) starting with the single-look complex images from ESA and JAXA. Stack processing was performed with ISCE on two of the Sentinel-1 tracks descending track D098 and ascending track A135, for all data from July 2019 through early August 2020. Time series analysis was conducted with MintPy (Yunjun et al., 2019) to reconstruct the LOS displacements for all the dates on each track and to estimate the coseismic step functions at the times of the $M_w 6.4$ January 7, 2020 earthquake and the events around July 3, 2020 and better separate the earthquake deformation from atmospheric effects (Fielding et al., 2017). We processed wide-swath (ScanSAR) data from ALOS-2 to form a coseismic interferogram on descending path 135 using the ALOS-2 application in ISCE2 (Liang & Fielding, 2017).

We combined LOS displacement estimates from the step-function fits to the Copernicus Sentinel-1 time series. The LOS (ground-to-satellite vector) for the Sentinel-1 ascending track A135 is up and slightly north of due west, while the LOS for the descending track D098 is up and slightly north of due east. We used the same reference point at 18.0°N and 67.0°W for both tracks. The displacements are set to zero at the reference point, and all the other displacements are given relative to this point. We can combine the two InSAR LOS measurements to estimate two components of the surface displacements that are close to east and vertical but contain a small percentage of north displacement (Wright et al., 2004). The resulting estimate for the near-vertical component of coseismic displacement was contoured. The estimated vertical component of coseismic displacements due to the $M_w 6.4$ January 7, 2020 is the difference between the time series step-function at the interval between January

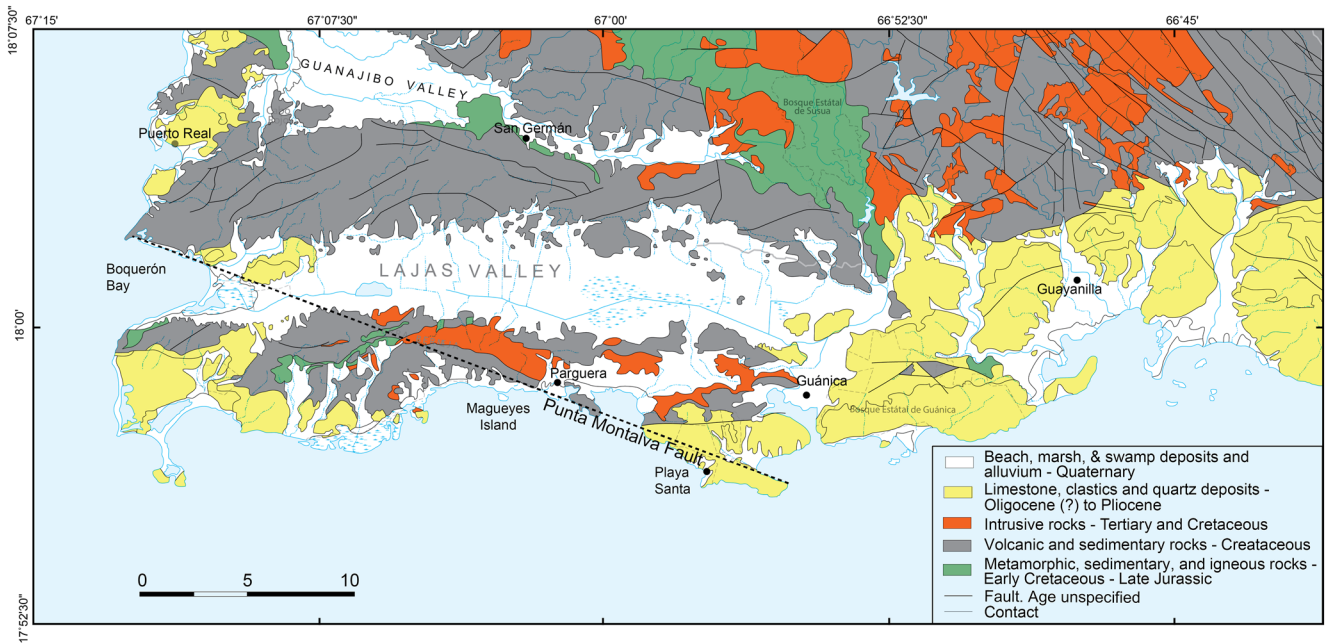


Figure 3. Simplified geological map of southwestern Puerto Rico modified from Renken et al. (2002). Dotted line – proposed 33-km-long Punta Montalva Fault by Roig-Silva et al. (2013).

2 and 14, 2020 and are shown as red contours on Figure 5. The near-horizontal component is smaller than the vertical and is not shown.

We did a similar step-function fit to the two Sentinel-1 time series for July 3, 2020. As with the January step-function fit, the 12-day intervals between acquisitions on the two Sentinel-1 tracks means that all deformation in the time between acquisitions cannot be separated. For the A135 track, the interval that contains July 3 was July 2–14 and for the D098 track, the interval was June 30 to July 12. The conversion to near vertical and east components assumes that the surface displacements are the same in the two step-function fits, which should be accurate if nearly all the displacement was between July 2 and 12. This interval includes several earthquakes; the largest were a pair of Mw4.9 and 5.3 on July 3. The estimated near-vertical component is shown in Figure 6. An area of coastal subsidence that is much smaller than the Mw6.4 signal was detected near Playa Santa that may be due to one of the Mw4.9 or the Mw5.3 July 3 earthquakes offshore (Figure 6). The subsidence was accompanied by near-westward horizontal component west of Playa Santa and a near eastward component east of Playa Santa.

High-quality cGPS time series relative to the Caribbean reference frame for 9 stations surrounding the study area (Figure 1) were downloaded from the Nevada Geodetic Laboratory (Blewitt et al., 2018). We used the data that was processed using final GPS orbits. The time series were used to evaluate relative plate motions within the region and encompassed available continuous observations for at least 4 yr since 2008 and prior to the start of the seismic sequence.

Locations and focal plane solutions of $M_w \geq 4.5$ earthquakes in this sequence, published by the Advanced National Seismic System (ANSS) Comprehensive Earthquake Catalog (ComCat; <https://earthquake.usgs.gov/earthquakes/search/> accessed February 15, 2021) have been adopted for analysis here.

The epicenter of small earthquakes in Figure 2 were relocated using the HypoDD algorithm (Waldhauser & Ellsworth, 2000) using the Puerto Rico Seismic Network (PRSN) P and S arrival pick data between December 15, 2019 and August 19, 2020. The parameters applied in the relocation were as follows: maximum separation distance of 7 km, minimum of 16 observations per event, and a minimum of 12 pairs. With these constraints, 7,130 earthquakes were retained for relocation (Vanacore et al., 2021).

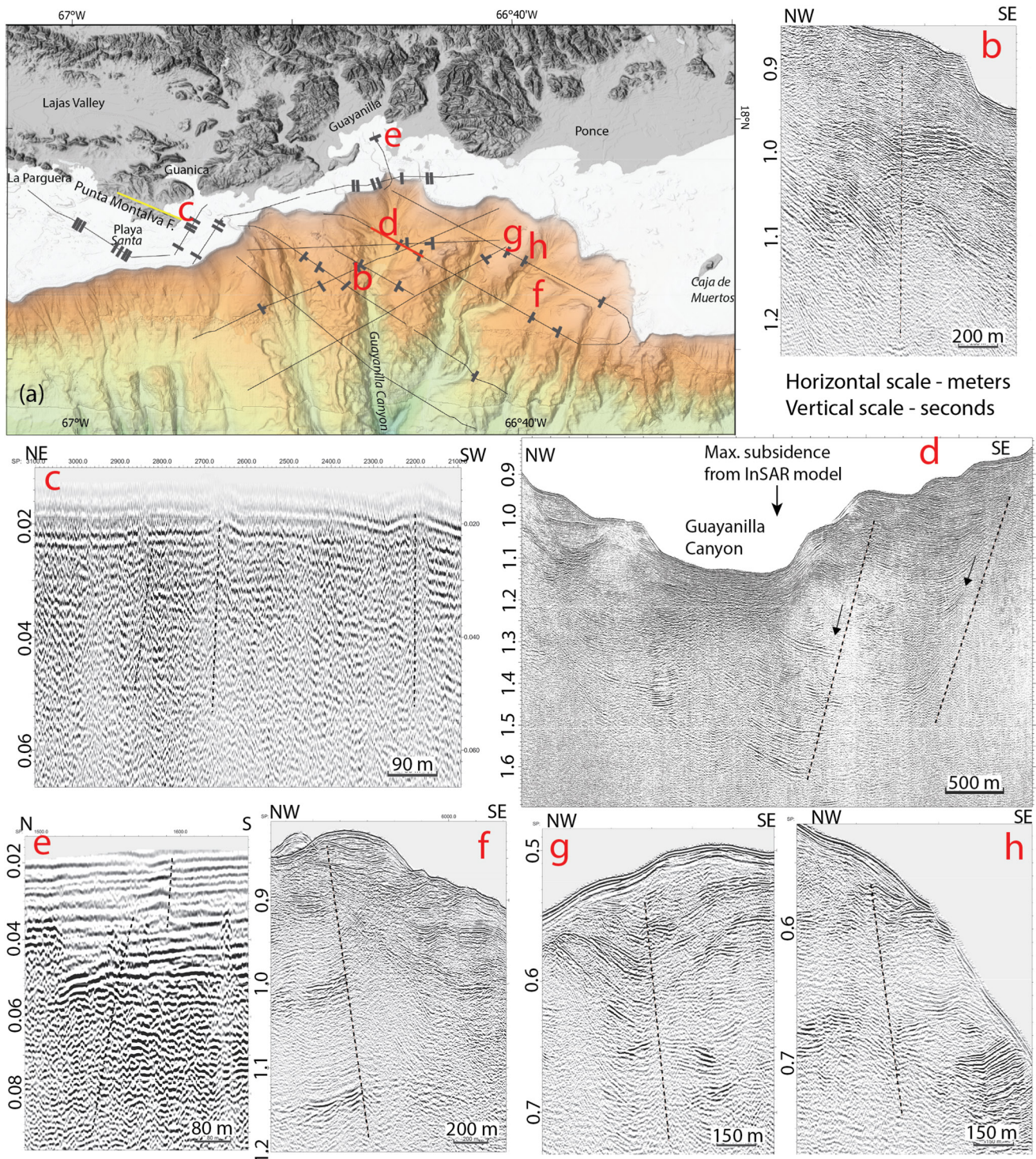


Figure 4. (a) – Location map of seismic records shown in (b–h). Red line shows extent of profile (d). (b–h) examples of interpreted faults (dashed lines). (d) – tilted reflectors toward the faults. The maximum sediment thickness is coincident with the region of maximum subsidence predicted by the Mw6.4 subsidence model. White area on map (a) is the shelf with water depths <100 m, above which limited sound source output was used and seafloor was typically made of hard coral reef. Thin lines in (a) – locations of seismic reflection profiles. Heavy black marks in (a) – Interpreted faults on the seismic reflection profiles with small perpendicular marks denoting apparent dip direction. Vertical scale of 0.1 s of two-way travel time in (b–h) corresponds roughly to 100 m in the sub-seafloor.

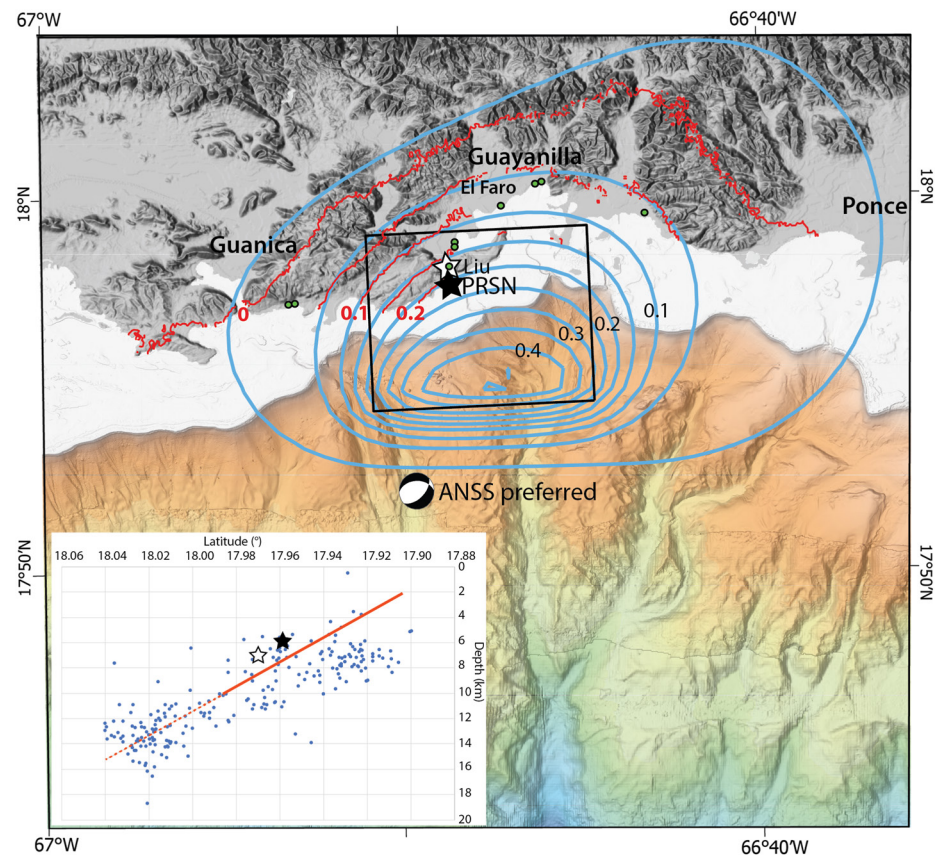


Figure 5. Comparison between Synthetic Aperture Radar interferometry subsidence observations for the period January 2–14, 2020 (red contours) and the subsidence model discussed in the text (blue contours). Contour interval for both is 0.05 m. Black rectangle – Surface projection of the modeled fault plane. The fault plane dips 43° to the north. See Text and Tables S3 and S4 in Supporting Information S1 for modeled fault parameters. Note that the preferred epicenter in the ANSS-ComCat is 5 km south of the updip edge of the fault plane, whereas the PRSN epicenter is located toward the bottom of the fault patch. Liu – Liu et al. (2020) epicenter (17.97°N, 66.81°W). Green dots – reported locations of coastal subsidence following the earthquake. Inset – Projection of relocated small earthquakes by Vanacore et al. (2021) occurring within the longitudes of the modeled fault patch during January 7–8, 2020. Red line is our modeled fault plane. Dashed red line is an extrapolation to deeper depths. Black and white stars – Projected hypocenters of PRSN and Liu et al. respectively.

4. Observations and Modeling

4.1. Seismic Reflection

Faulting was interpreted in the seismic profiles where relatively continuous reflectors were offset by discontinuities and diffractions. Faults were typically characterized by zones of opaque reflectivity extending sub-vertically for a few hundreds of milliseconds (Figure 4). The observed faults typically do not offset the seafloor but end a few tens of milliseconds below it. The faults we mapped are concentrated in three specific areas. Most of them are distributed 3.5–7 km seaward of the shelf edge between Guayanilla and Guanica (Figures 2 and 4). Two additional fault groups were identified, one on the slope SW of Ponce Basin (Figures 4f–4h), and the second group at distances of 17–21 km from the shelf edge. Fault zones were not identified elsewhere in the survey area, that is, closer to the shelf edge or in the zone between 7 and 17 km from the shelf edge. Apparent dips of the mapped fault zones range from ~45° to sub-vertical.

The insular shelf platform is typically <20 m deep, is rimmed by modern fringing reefs at the shelf edge, and is mantled by patch reefs, cays, and pavement-encrusted coralline algae, stony corals (*Scleractinia*) and sponges (Ballantine et al., 2008). The cays and shallow shoals are hazards to navigation and interfered with data acquisition.

Seismic profiles collected on the shelf were of low-quality relative to deeper offshore profiles due to greater noise and limited penetration of the seismic energy. Accordingly, it was challenging to distinguish between folds, the

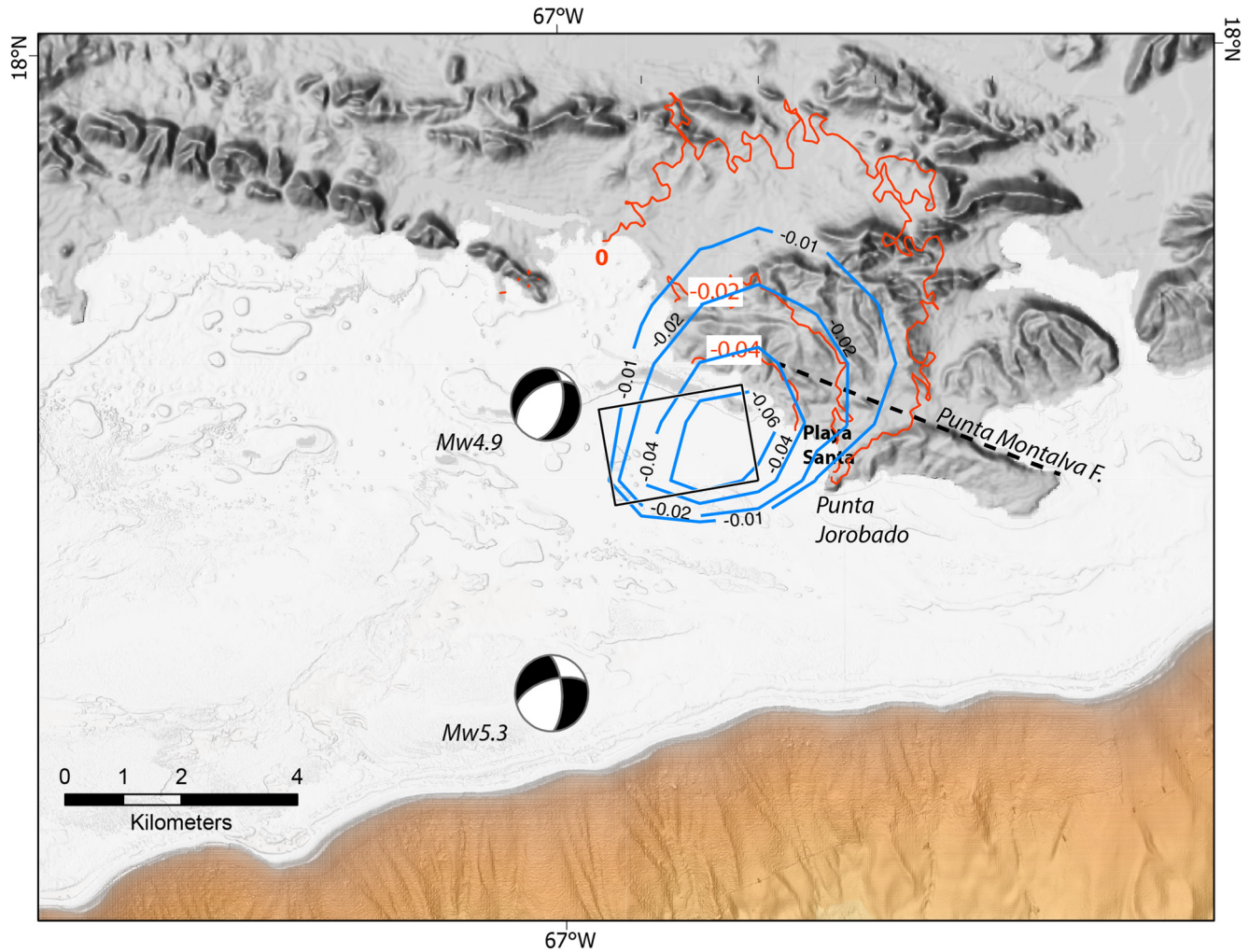


Figure 6. Comparison between Synthetic Aperture Radar interferometry subsidence observations during the period of July 2–12 (red contours) and modeled subsidence using the modified ANSS-ComCat focal plane parameters for the Mw5.3 (blue contours). Contour interval for both is 0.02 m. Black rectangle – Surface projection of the modeled fault plane. Fault plane dips to the NW. See Text and Table S5 in Supporting Information S1 for modeled fault parameters. Beach balls – Focal mechanisms for the two July 3, 2020 earthquakes are from ANSS-ComCat listed in Table S1 in Supporting Information S1.

irregular boundaries separating reefs from adjacent inter-reef sediment-filled depressions, and offsets or disturbances of horizontal reflectors that may be indicative of faults. However, sub-vertical fault traces were identified in a few locations (Figure 4). Faults were interpreted in two parallel seismic lines offshore Punta Montalva, one in the vicinity of the offshore continuation of Punta Montalva Fault, and a second farther south (Figures 2 and 4c). Faults were also identified on the shelf within (Figure 4e) and seaward of Guayanilla Bay, as well as south of Playa Santa and La Parguera.

4.2. Surface Subsidence and Displacement

Eyewitnesses reported permanent flooding of parts of El Faro (Figure 5), a coastal community in Guayanilla, immediately following the Mw6.4 event (Pérez-Valentín et al., 2021). Permanent flooding was also documented in other coastal locations in surveys conducted during the week following the earthquake (green dots in Figure 5; Allstadt et al., 2020). Subsidence during the time interval of January 2–14, 2020 with a maximum of 20 cm was observed in InSAR time series and, based on the eye-witness reports, was assumed to be due to the Mw6.4 January 7, 2020 (Figure 5). The long axis of the subsidence is oriented in a NE-SW-direction with amplitude increasing offshore. We forward modeled vertical subsidence with Coulomb 3.3 software (Toda et al., 2011) assuming an elastic half-space and using the focal plane parameters for the Mw6.4 earthquake reported by the

ANSS-ComCat (strike, dip, rake, and seismic moment of 268° , 43° , -58° , and 5.04×10^{18} N-m, respectively). The fit of the model to the shape of the observed subsidence anomaly was significantly improved when a rake of -72° was used instead of -58° (i.e., a relatively larger normal component and smaller left-lateral component than the ANSS solution). Trial-and-error modeling of the rupture length, width, and slip, which conform to the seismic moment provided by ANSS-ComCat, resulted in the best qualitative fitting model of top and bottom depths of 2 and 10 km, rupture length of 11.3 km, and a uniform slip of 1.265 m. These values are close to those of Liu et al. (2020) who estimated peak slip of 1.6 m and main slip patch between 3 and 13 km from kinematic inversion of GPS and strong motion data. Our model used the typical crustal shear modulus of $\mu = 30$ GPa. Our best-fit model predicts a maximum subsidence of 0.45 cm offshore centered at the upper reach of Guayanilla Canyon (Figure 5).

The location of our modeled fault plane (rectangle in Figure 5) and its dip also match the relocated micro-seismicity by Vanacore et al. (2021) from January 7 to 8, 2021 (the rupture day and the following day; Inset in Figure 5). Micro-seismicity on January 7, 2020 prior to the Mw6.4 earthquake was limited to depths <8.5 km but extended downward to ~ 15 km after the event, suggesting that the rupture continued to propagate deeper.

The ANSS-ComCat preferred earthquake epicenter falls, however, outside the surface projection of the fault plane (Figure 5), but an alternate epicenter determined by the PRSN and listed in the ANSS-ComCat (17.9578°N , 66.8113°W , Table S1 in Supporting Information S1) is located near the bottom edge of the modeled slip patch (Star in Figure 5 and in inset). Similarly, the PRSN alternate epicenter of the January 6, 2020 Mw5.8 earthquake, which was thought to trigger the Mw6.4 earthquake is located within the modeled fault patch, whereas the preferred ANSS-ComCat location is 5 km to the south.

A second much smaller coastal subsidence (≤ 0.04 m) was detected near Playa Santa from the InSAR time series fit for the period between July 2 and 12, 2020 (red contours in Figure 6). Two offshore moderate-size earthquakes occurred during this period, an Mw5.3 July 3 (primarily left-lateral strike-slip) and an Mw4.9 July 3 (primarily normal) closer to shore. The subsidence was accompanied by horizontal displacement with opposing directions west and east of Playa Santa and a maximum amplitude of 8 cm. However, the InSAR anomaly cannot distinguish between east and north displacements, because the satellite lines-of-sight in this area are primarily east and west. Additionally, GPS data from station PRMI (Nevada Geodetic Laboratory, Blewitt et al., 2018; Figure 1) document a step-change in the horizontal displacement components around July 3, 2020 with the north component being almost double the east component. We, therefore, limited our modeling to the near-vertical InSAR subsidence anomaly. The near-vertical subsidence was modeled with Coulomb 3.3 software (Toda et al., 2011) using the focal parameters published in the ANSS-ComCat for both the Mw5.3 and Mw4.9 that occurred during the observation period (Table S3 in Supporting Information S1). Because the preferred focal plane parameters in the catalog produced significant misfits to the observations, we tested the alternate focal plane parameters provided in the catalog varying only the top and bottom depths of the fault, its average slip, and its location. The trial-and-error model that qualitatively best fits the observed subsidence is shown in Figure 6. It uses the alternate focal plane parameters for the Mw5.3, and the fault plane is shallow (0.5–3.5 km). The shallow depth is compatible with the origin depth in the ANSS-ComCat (3 km) but the modeled fault plane is located closer to shore than the published epicenter (Figure 6). The mixed left-lateral and normal motion (rake of -27°) of the qualitative best-fit subsidence model may indicate that the Punta Jorobado peninsula (Figure 6) has formed as a result of recurring earthquakes with a similar sense of motion.

5. Interpretation

5.1. Seismic Reflectors

Seismic reflection profiles crossing the insular slope show patches of surficial sediment cover spanning ≤ 0.05 s two-way travel time (<50 m assuming seismic velocity $<2,000$ m/s) except where deposited in depressions on the flanks of canyon interfluves (Figure 4). The underlying reflectors are discontinuous, either because of poor acoustic penetration or due to collapse and tilting of small blocks, the latter being observed onshore (Mann et al., 2005; Monroe, 1980; Renken et al., 2002). The ages of these reflectors cannot be precisely determined without borehole data.

Tilted seismic reflectors were observed to increase in thickness toward the south in the vicinity of the headwater of the Guayanilla Canyon (e.g., southward tilting reflectors toward the faults in Figure 4d), which may represent

an asymmetric depocenter. This depocenter is located in the region of maximum subsidence from modeling the InSAR data (Figure 5). The density and orientation of the seismic profiles do not allow us to map the extent of the region of tilted reflectors with confidence. The internal stratigraphy of the tilted reflector geometry is discontinuous and does not allow us to determine if the reflectors fan out representing constant sediment supply to the depocenter during tilting and subsidence. It is also possible that sediment supply does not keep up with subsidence and/or the sediments are being transported to deeper water.

5.2. Associating Mapped Faults With Seismic Events and Fault Planes

Fault parameters such as dip, strike, and rake cannot be deduced from the profiles, because of the sparse line distribution and because shallow deformation in relatively poorly consolidated sediments is often not indicative of fault parameters at depth (e.g., Harding, 1985; Withjack et al., 1995). The lack of seafloor offsets associated with the sub-vertical faults in the seismic profiles either indicates that these fault zones have not been active during the most recent seismic activity or that the shallow sub-seafloor sediments are unconsolidated and do not deform in a brittle fashion (e.g., Kaneko & Fialko, 2011). In places (e.g., Figures 4b and 4g), we do observe shallow sediments that consist of landslide debris unconformably overlying the deeper sediments, which supports the latter hypothesis.

We next try to associate the locations of observed faults with specific clusters of earthquakes and with fault planes derived from the InSAR data. The spatial distribution of the mapped faults, mostly close to the shelf edge, and rarely or not in deeper water, is similar to the spatial distribution of the 2020 seismic sequence, suggesting that earthquake activity in the region has in the recent geologic past been probably limited to the nearshore area. More specifically, the belt of observed faults 3–7 km south of the shelf edge in the seismic data could correspond to the shallow strain relief associated with the Mw6.4 rupture (blue rectangle in Figure 2b) and/or the rupture of other earthquakes before and after this earthquake (Figures 2a and 2b). The faults on the shelf south of Guayanilla Bay may all be pre-existing, but also could have been reactivated or may be new faults that formed during the January 7, 2020 Mw6.4 earthquake or the January 20, 2020 earthquake cluster (green in Figure 2c). The fault in the middle of Guayanilla Bay (Figures 2c and 4e) may be the extension of one of the faults crossing the bay from west to east (Grossman, 1963;). A better delineation of this fault is needed because of its location under a population center and critical industrial facilities.

However, the association of other observed faults in the seismic reflection data with the locations of moderate or large earthquakes is less straight forward. Several faults were observed SW of Caja de Muertos Fault and Ponce Basin, but moderate-size seismic activity did not extend to that area (Figure 2). Whether this area is still seismically active, is unknown. One possibility is that these faults undergo shallow creep induced by nearby large earthquakes existing faults. An example of such phenomenon (although on an active fault) is the observed shallow creep deformation on the Garlock Fault, California, following the Ridgecrest earthquake 5–20 km away (Ross et al., 2019).

5.3. The Role of Punta Montalva Fault in the Seismic Sequence

The Punta Montalva Fault was proposed by Roig-Silva et al. (2013) to be an active strike-slip fault extending for 33 km from the tip of Punta Montalva northwestward to Boquerón Bay (Figure 3) This proposed fault appears, however, to have had a little role in the initiation of the 2019–2020 seismic sequence, which started several km ENE of the southeastern end of the fault (Figure 2a). Only during June 2020, five months after the January 7, 2020 Mw6.4 earthquake, did moderate-sized strike-slip earthquakes take place onshore along the southeastern-most 5-km of the fault (Figure 2d). Adames-Corraliza (2017) considered this 5-km-long onshore fault segment to be active based on offset measurements made from LIDAR and Ground Penetrating Radar data. The majority of the proposed fault to the northward was not associated with either moderate earthquakes or with microseismicity during the 2019–2020 seismic sequence (Figure 2). The role of the Punta Montalva fault in accommodating the differential block model in SWPR, therefore remains unknown. An evaluation of the potential seismic activity along the entire 33-km-long strike-slip fault is important because rupture of the entire length can generate an M6.9 earthquake (Wells & Coppersmith, 1994).

5.4. Progression of Seismic Activity

Moderate-size ($\geq M_w 4.5$) earthquake activity shows a complex temporal development of both strike-slip and normal faults. Figure 2 shows our interpreted color-coded clusters with their temporal progression following the color spectrum from purple to red (inset in Figure 2a). Epicenters of small earthquakes relocated using the HypoDD algorithm (Vanacore et al., 2021) that took place during most of the dates of moderate-size earthquake activity were plotted with colors similar to their respective moderate-size earthquakes. Their distribution provides the spatial context to the ruptures associated with moderate-size earthquake activity.

Earthquake activity started SE of Guayanilla on December 28, 2019 and advanced to the SE along one or more faults by $M_w \leq 5$ earthquake having left-lateral strike-slip focal mechanisms (Figure 2a). This activity triggered an $M_w 5.8$ strike-slip earthquake on January 6, 2020, which was located within the patch of the January 7, 2020 $M_w 6.4$ fault plane modeled from the InSAR subsidence. The $M_w 6.4$ in the early morning of January 7, 2020 occurred within this patch and additional normal and strike-slip ruptures extended SE and north of the patch, perhaps along secondary faults (Figure 2b). Normal and strike-slip fault ruptures, including an $M_w 5.9$ earthquake, took place along the western side of the $M_w 6.4$ patch 3–7 days later (January 10–14, 2020) and were accompanied by intense micro-seismicity along a 20-km-long NNE-SSW-oriented belt (blue dots in Figure 2c). However, the locations and focal mechanisms of moderate earthquakes during this period indicate that this belt of seismicity is not a single fault. Normal fault ruptures on January 20, 2020 (green in Figure 2c) and east of it on May 2, 2020 (yellow in Figure 2d) took place along the eastern edge of the $M_w 6.4$ rupture plane. Left-lateral strike-slip earthquakes took place along the NE and western edges of the patch on August 7, 2020 (brown in Figures 2d) and December 24, 2020 (dark gray in Figure 2d). Seismic activity intensified 10–15 km west of the $M_w 6.4$ rupture plane during June–July 2020 with some events probably occurring along the SE section of Punta Montalva Fault (orange in Figure 2d) and others under the shelf (red in Figure 2d). The latter events were probably associated with the small coastal subsidence and horizontal motion, detected by InSAR, which was discussed in Section 4.2 and Figure 6.

Several inferences can be drawn from this sequence of events: First, the sequence is not a typical foreshock-main-shock-aftershock sequence. We base this inference on two lines of evidence: (a) The magnitudes of the seismic sequence did not follow Båth's Law (see inset in Figure 2a). Båth's Law states the largest aftershock is 1–1.2 magnitude levels smaller than the main shock (e.g., Shcherbakov & Turcotte, 2004). (b) The energy released during the January 7, 2020 $M_w 6.4$ earthquake was only 64% of the total energy released during the seismic sequence, assuming similar stress drops during all the earthquakes. Second, the area may be crisscrossed by intersecting network of short faults, which were probably activated in a complex way by the changing stress field caused by the progression of rupture along different faults. Third, the earthquake sequence was probably initiated by offshore strike-slip fault(s) SE of Guánica (Figure 2a), and not by rupture on the Punta Montalva Fault as initially proposed (López-Venegas, Vanacore, Hughes, Báez-Sánchez, et al., 2020). Moderate earthquakes on the Punta Montalva Fault occurred only during June–July 2020 late in the seismic swarm sequence.

6. Discussion

6.1. Longer Term Tectonic Activity

Several lines of evidence indicate that the seismic sequence in SWPR is but the latest episode of a repetitive earthquake cycle, whose recurrence interval is unknown. The extension directions indicated by the T -axis analysis of moderate ($M \geq 4.5$) earthquakes from the ANSS-ComCat ($329^\circ \pm 10^\circ$; heavy double-sided arrows in Figure 7, Table S1 in Supporting Information S1) are similar to those derived by Mann et al. (2005) from the study of terrestrial fault striations in the area (303° – 344° ; double-sided blue arrows in Figure 7). The age of the terrestrial faults is estimated at post-early Pliocene based on cross-cutting relationships with older faults (Mann et al., 2005).

The area of seismic activity is the only part of southern Puerto Rico where the shelf is indented northward, and the shelf edge becomes as narrow as 1 km (Figure 7). The subsidence model for the January 7, 2020 $M_w 6.4$ earthquake predicts the location of maximum subsidence to be at the headwaters of this canyon (white star in Figure 7), and recurrent rupture of these faults could have helped create the shelf indentation in this area.

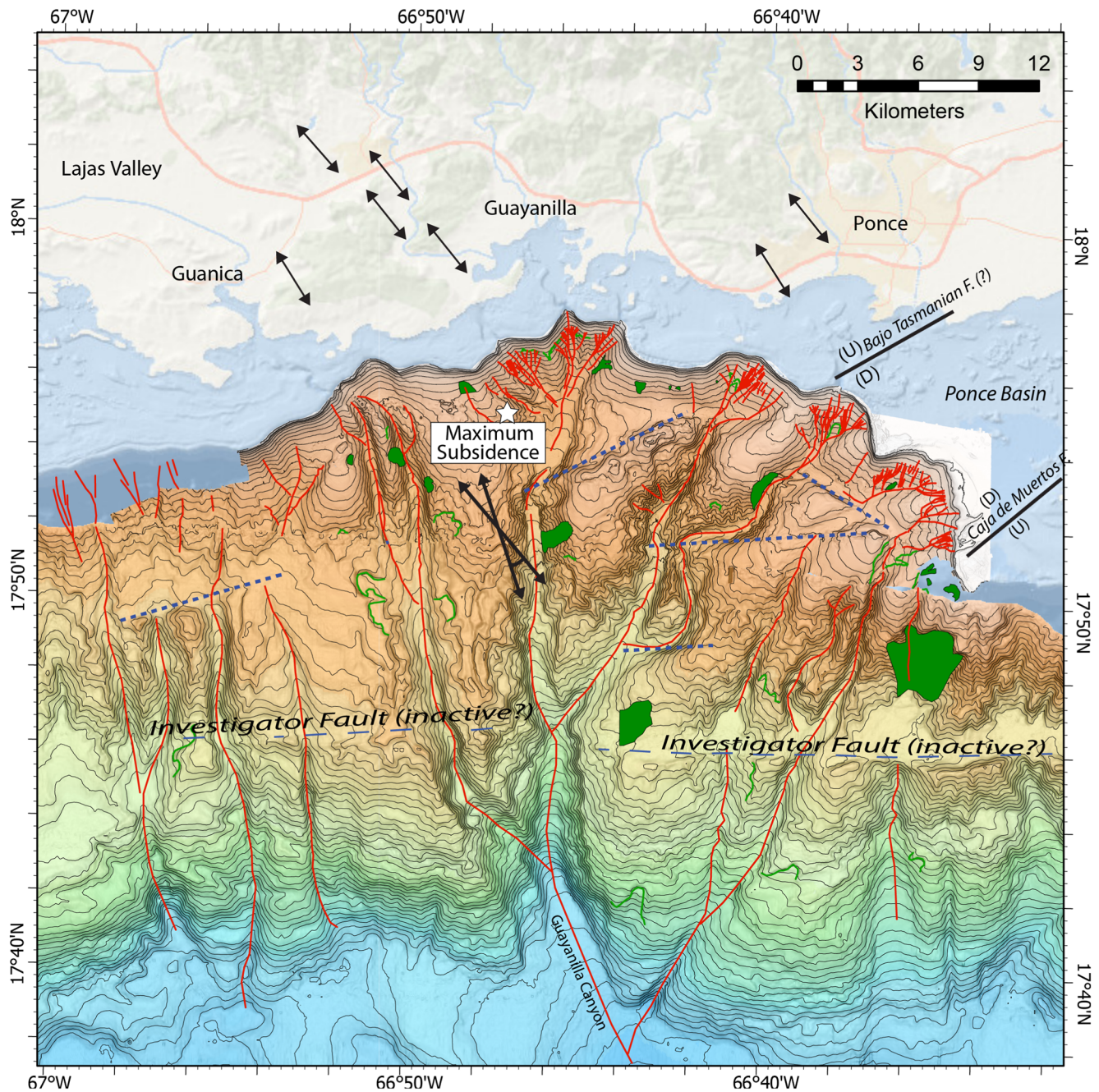


Figure 7. Compilation of evidence suggestive of long-term seismic activity in the study area. Dark double-sided arrows – Extension directivity of a range of T -axes for $M_w > 4.5$ earthquakes in the seismic sequence (shown offshore; See Table S1 in Supporting Information S1). Double-sided blue arrow – Extension directions from terrestrial post Early Pliocene fault striations (Mann et al., 2005). Yellow lines – mapped faults enclosing the several hundred milliseconds thick Ponce half-graben and their sense of motion (Garrison, 1969). Star – Center of modeled subsidence in Figure 5. Blue dashed lines – Seafloor lineaments disrupting drainage on an otherwise general southward slope indicating possible tectonic control. Red lines – Thalwegs of the drainage system. Green areas – Landslide scars. Green lines – Landslide scarp. Guayanilla Canyon is the only large submarine canyon along southern Puerto Rico, and it eroded the shelf to within 1 km from shore.

We interpret the tilted geometry of the sedimentary fill (Figure 4d) to be the result of an episodic rupture (or creep) of a normal fault(s), such as the one hosting the $M_w 6.4$ earthquake, which progressively down throws the north side of the fault(s) and traps sediments into an asymmetric depocenter. The observed thickness of the depocenter, at least 0.5 s (~500 m), suggests that the depocenter had developed over a significant time period. The depocenter is collocated with region of maximum subsidence due to the $M_w 6.4$ earthquake, modeled from

the InSAR data. The recurrence interval of earthquakes similar to the Mw6.4 earthquake is unknown, but if its average slip (1.27 m) is representative, then the depocenter developed over hundreds of earthquake cycles.

The bathymetry also shows two NE-oriented bathymetric lineaments that are deeper to the NW despite the general southward dip of the insular slope (dashed blue lines in Figure 7). These lineaments, and the down-to-the-NW normal displacement of many of the earthquakes' focal mechanisms, including the largest Mw6.4 event, suggest relative subsidence close to shore and relative uplift farther away from shore toward the SE.

The area of seismic activity is located at the headwaters of the only large submarine canyon along southern Puerto Rico, the Guayanilla Canyon. Given the lack of major terrestrial rivers feeding the canyon system, the canyon system has likely developed to evacuate the sediments of the collapsing shelf edge by repeated normal faulting. The canyon system itself might have been partially affected by the repeated seismic activity, as is evident by the curious right-angle meandering of the eastmost tributary of the canyon. These abrupt meanders may be controlled by subsurface faults (dashed blue lines in Figure 7). Since submarine morphology typically develops over a long geological time, the presence of the shelf indentation, unique lineaments, and meanders are other indicators for a long-term history of seismic activity.

6.2. Diffuse Tectonic Boundary

The convergence rate and azimuth of the North American Plate with the Caribbean Plate is relatively constant across the span of the 800 km of the Puerto Rico Trench with deviations arising only from local variability in plate boundary orientation (Figure 1). Nevertheless, seismic coupling appears to vary significantly across the plate boundary. The sector from the longitude of Mona Rift westward (Henceforth, Hispaniola) is associated with several large 20th century earthquakes (e.g., ten Brink et al., 2011), with partitioning of the GPS motion between sub-perpendicular convergence and sub-parallel strike-slip, and with the accumulation of large strains on the upper plate (Symithe et al., 2015). The sector east of the longitude of Mona Passage (henceforth, Puerto Rico) is associated with smaller earthquakes, many of them showing oblique-slip sub-parallel to the convergence direction (ten Brink, 2005; ten Brink et al., 2011). GPS velocities in Puerto Rico relative to the Caribbean plate are 1/5 those in Hispaniola, likely because of significant differences in coupling across the subduction interface between the Puerto Rico and Hispaniola segments of the trench (Figure 1; Symithe et al., 2015; ten Brink & López-Venegas, 2012).

The difference in azimuth and magnitude of the GPS velocity between Puerto Rico and Hispaniola suggests the presence of a boundary between the upper plate blocks of Hispaniola and Puerto Rico. This boundary crosses the ancient island arc, but its location and nature are poorly defined. Kinematic block models provide a relative block motion estimate of 1–5 mm/y (e.g., Symithe et al., 2015). Manaker et al. (2008) and Mann et al. (2002), and others suggested that the boundary connects Mona Rift to Yuma Basin. Detailed multibeam bathymetry and seismic reflection mapping show a system of WNW-ESE normal faults with a nested fault-system oriented NW-SE exposed at the seafloor, which presumably indicates neo-tectonic NE-SW motion across the boundary (Chaytor & ten Brink, 2010). ten Brink and López-Venegas (2012) using GPS measurements between 2008 and 2011 noted that stations PRMI in SWPR and MOPR on Mona Island (see Figure 1 for location) move in the direction of Hispaniola whereas stations farther to the north and to the east move with the direction of the Puerto Rico block. They also noted a seismicity belt extending from Mona Rift to the SE through southwest PR. Solares-Colón (2019) used the *F*-test to support the independent motion of SWPR recorded by GPS with respect to the Puerto Rico block, and its similar direction to Mona Island and eastern Hispaniola. The width of the accretionary wedge of Muertos Trough changes significantly at the longitude of the SW corner of Puerto Rico (Granja-Bruña et al., 2009). The change in the width of the accretionary prism may correspond to the location of the block boundary, assuming that the Muertos accretionary prism is a back-arc wedge of the Puerto Rico-Hispaniola subduction zone (ten Brink et al., 2009).

Elastic strain commonly accumulates in the locked parts of the subduction interface during inter-seismic times dragging the upper plate in the direction of subduction at a significant fraction of the subducting plate velocity (Figure 8b). GPS velocities in Hispaniola show a southwestward azimuth sub-parallel to and at a significant fraction to the incoming North American plate. GPS velocities in Puerto Rico and the Virgin Islands, are in contrast, significantly slower than the incoming plate velocity and are oriented WNW, that is, their north component is opposite to the subduction direction (Figure 1). The GPS velocities in Puerto Rico and the Virgin Islands were

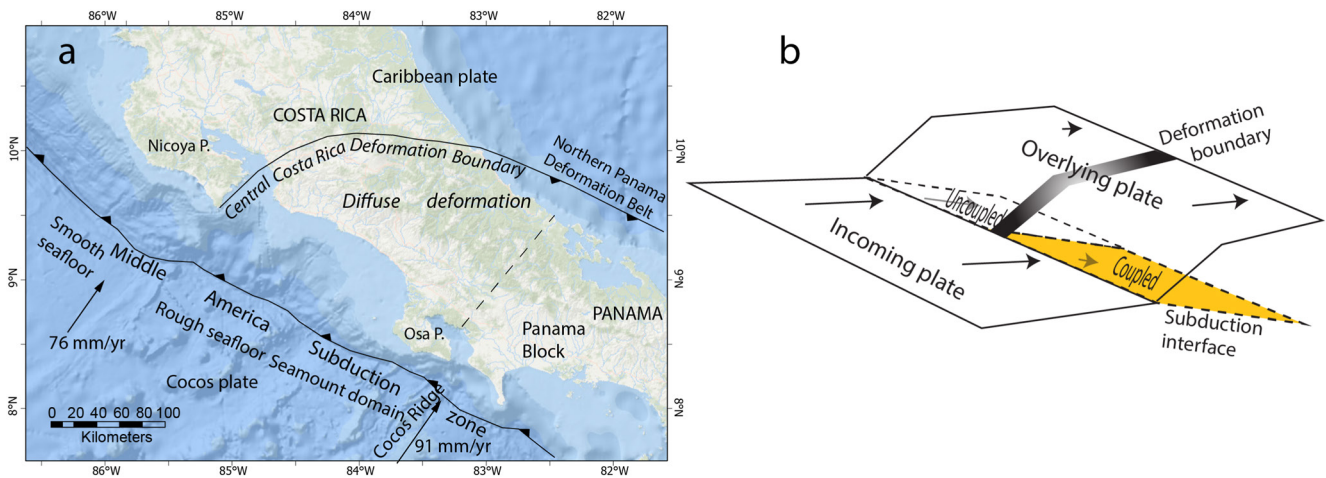


Figure 8. (a) Simplified map of the Central Costa Rica Deformation Boundary (Marshall et al., 2000), a diffuse block boundary, an analogous setting to the Western Puerto Rico Deformation Boundary. (b) Cartoon showing the impact of seismic coupling along the subduction interface on differential velocity of the overlying arc relative to the overlying plate interior. The coupled and uncoupled subduction interfaces are the Hispaniola and Puerto Rico segments, respectively, and are separated by a deformation zone north of Mona Rift. In Central America, the coupled and uncoupled subduction interfaces correspond to the rough and smooth seafloor of the incoming Cocos plate (a).

interpreted to indicate very low coupling across the subduction interface north of these islands (ten Brink & López-Venegas, 2012). We propose that the Western Puerto Rico Deformation Boundary (Figure 1) is driven by variations in seismic coupling on the Puerto Rico subduction interface, with high coupling north of Hispaniola and Mona Passage and almost no coupling north of Puerto Rico (Symithe et al., 2015). The deformation boundary may have several deformation domains: Mona Rift in the north is a classical rift graben bounded by a fault on its east side and perhaps another one on its west side. Mona Passage farther south exhibits NW-SE series of faults, many of them not organized in a uniform fashion (Chaytor & ten Brink, 2010). Some of these faults may extend eastward on land (Grindlay et al., 2005). SWPR is characterized by subdued topography and east-west valleys (e.g., Lajas Valley) and faults (Prentice & Mann, 2005). The recent seismic activity, reported here, describes an NW-SE extension offshore SWPR. It may connect to the Muertos back-arc accretionary wedge, which is significantly wider west of the deformation boundary.

We suggest that the Western Puerto Rico Deformation Boundary is similar to a diffuse zone of deformation observed in the Middle America arc (Marshall et al., 2000). Marshall et al. (2000) suggested that a change in coupling at the subduction interface is associated with a change from a smooth subducting seafloor offshore Nicaragua and northwestern Costa Rica to a rough seafloor in southeastern Costa Rica and Panama (Figure 8a). This lateral change in coupling, they hypothesized, causes differential movement of the arc with respect to the interior Caribbean plate, which is accommodated by a diffuse region of deformation, named Central Costa Rica Deformation Boundary (Marshall et al., 2000). It also affects the development of a back-arc accretionary wedge north of southeastern Costa Rica and Panama, known as the Northern Panama Deformation Belt (NPDB), which overthrusts the Caribbean plate. The Central Costa Rica Deformation Boundary exhibits several faulting domains with different faulting styles, recurring cycles of small and moderate earthquakes, and a change in the magnitude and orientation of the GPS velocity vectors from the Caribbean plate across the zone of diffuse deformation and to the Panama Block. Some of the seismic cycles in the deformation boundary have been triggered by large subduction or back-arc earthquakes.

Similar elements can be found along the Puerto Rico-Hispaniola inactive arc. Coupling of the subduction interface north of Puerto Rico appears low whereas west of Mona Rift and along the Hispaniola sector of the trench, coupling is high (e.g., Symithe et al., 2015). The collision of the thick crust of the Bahamas Bank with the subduction zone north of Hispaniola may play a major role in the high seismic coupling along this sector. Differential coupling across the subduction zone creates an irregular boundary across the volcanic arc, which exhibits diffuse deformation. Muertos thrust belt is well developed south of Hispaniola and is poorly developed south of Puerto Rico (Figure 1; ten Brink et al., 2009) similar to the NPDB north of the rough seafloor of southeastern Costa Rica and Panama.

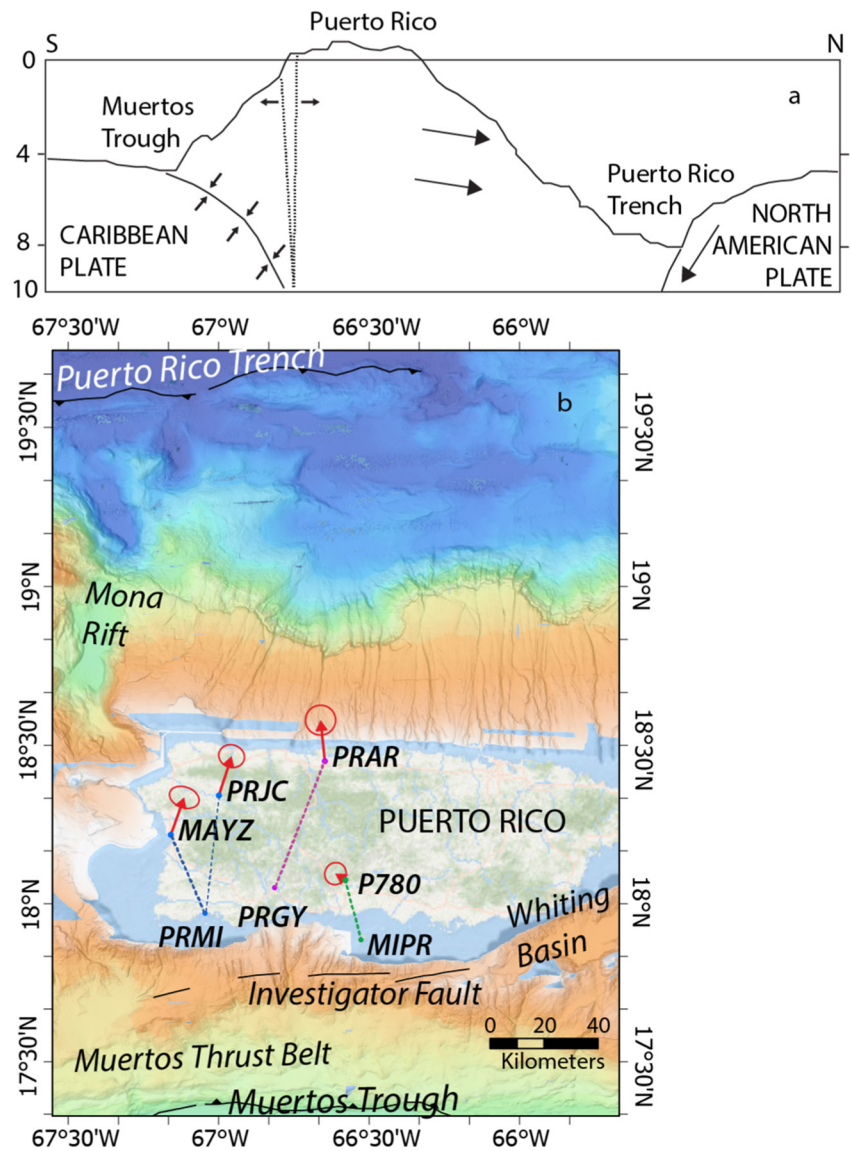


Figure 9. (a) An alternative explanation to the recent seismic activity in which fusion of the southern edge of the Puerto Rico block with the Caribbean plate while the rest of the block is dragged northward toward the trench may cause extension to develop along southwest Puerto Rico. (b) Velocity differences between GPS stations across Puerto Rico (Table S2 in Supporting Information S1). Red arrows show velocity vectors of stations relative to stations located farther south, with whom they are connected by dashed lines.

Alternatively, the seismic sequence of SWPR may perhaps be explained in the context of a slight north-south extension across the island arc in Puerto Rico, driven by strong coupling between the arc and the Caribbean plate interior and a weak coupling of the arc at the subduction zone to the north (Figure 9). Tilting and collapse of the forearc (ten Brink, 2005) would enhance upper crustal extension (Figure 9). Extension in the southern part of the arc is suggested by the basin morphology of Virgin Island Basin and Whiting Basin SE of Puerto Rico, and the possible extension across a narrow elongate bathymetric ledge (at the upper slope south of the island south of Puerto Rico (Investigator fault in Figure 7), sometimes named Investigator fault (e.g., Mann et al., 2005). SWPR also has a unique valley and range-like topography, indicating a relative north-south extension. The continuous pre-2020 high-resolution terrestrial GPS data (Table S2 in Supporting Information S1) also appear to indicate opposing roughly N-S motion between pairs of stations across the two blocks in question (Figure 9b).

6.3. Why Does Not the Deformation Zone Mature?

The recent seismic activity shows that despite being subjected to this tectonic/structural regime since perhaps post Early Pliocene, deformation continues to be accommodated along many small faults and has not coalesced into a mature boundary. We can offer several hypotheses to explain this observation. First, the rate of deformation at this boundary is low, perhaps 1–2 mm/y (1–2 km per Ma), and therefore, the coalescence of many faults into one or a couple of major faults may take a lot longer in the NE Caribbean. A second and perhaps more plausible hypothesis is that the inherited island arc structure and composition, such as in Puerto Rico (Figure 3) are anisotropic because the accretion and deformation processes are caused by inter-plate convergence. The anisotropic composition of the arc may promote long along-arc faults, such as strike-slip faults in oblique convergence regimes, and short faults with chaotic orientations at block boundaries across the arc. Observed upper plate deformation along the oblique Sumatra subduction zone is trench parallel and comprises of pervasive folds and thrust faults (Graindorge et al., 2008) and long strike-slip fault systems (Sumatran and Mentawai; Izzart et al., 1994; McCaffrey et al., 2000). Mapped cross-arc faults in Central Costa Rica Deformation Boundary, seldom span more than 20 km (Table 1 in Marshall et al., 2000).

7. Conclusions

The 2019–2020 SWPR seismic sequence ruptured multiple short normal and strike-slip faults along the insular shelf and upper slope of southwest Puerto Rico. The seismic activity included many moderate-size earthquakes over a span of a year and did not follow a typical main shock-aftershock sequence. InSAR-detected coastal subsidence, earthquakes clustered in time and space, and sub-seafloor faults, detected in high-resolution seismic reflection survey, attest to the existence of multiple rupturing faults at different orientations. Despite morphological and structural indicators of a long-term deformation history of similar nature, the deformation does not seem to center on one or more mature fault, perhaps because of the heterogeneous composition and structure across the arc. The 2019–2020 seismic sequence may be the southernmost domain of a diffuse deformation boundary between the Hispaniola and Puerto Rico blocks, which also includes the domains of corner of the southwestern Puerto Rico, eastern Mona Passage, and Mona Rift. The diffuse zone, which we name the Western Puerto Rico Deformation Boundary, may be analogous to the Central Costa Rica Deformation Boundary and may be driven by variations in subduction coupling along the Puerto Rico Trench.

Data Availability Statement

Seismic reflection data and navigation can be downloaded from <https://www.sciencebase.gov/catalog/item/60a2d-193d34ea221ce432fe5>. Earthquake data can be found in ANSS-ComCat <https://earthquake.usgs.gov/earthquakes/search/>. Table S1 in Supporting Information S1 lists the catalog parameters of earthquakes with $M_w \geq 4.5$ including alternative locations, plotted in Figure 2. GPS data can be found at <http://geodesy.unr.edu/magnet.php>. Table S2 in Supporting Information S1 lists the parameters of the stations appearing in Figure 1. Processed InSAR data can be found in https://aria-share.jpl.nasa.gov/20200106-Puerto_Rico_EQ/Displacements/. Original Copernicus Sentinel-1 data is available at no charge from the Copernicus Sentinels Scientific Data Hub (<https://scihub.copernicus.eu/>) and is mirrored at the NASA Alaska Satellite Facility archive center <https://search.asf.alaska.edu/>. Original ALOS-2 data is available from JAXA (<https://earth.jaxa.jp/en/research/cooperation/index.html>). Bathymetry data can be found in <https://doi.org/10.25921/ds9v-ky35> and Andrews et al. (2014). For further details see Text S1 in Supporting Information S1.

Acknowledgments

The logistical support of the University of Puerto Rico Department of Marine Sciences in carrying out a rapid response seismic reflection survey only two months after the largest earthquake in the sequence is greatly appreciated. The logistical support included the use of the R/V Sultana and shore support at the department's shore lab in Isla Maguëyes

References

- Adames-Corraliza, Á. R. (2017). *Geomorphic and geophysical characterization of the north Boquerón Bay-Punta Montalva Fault zone: A capable fault system in southwestern Puerto Rico*. Mayaguez. University of Puerto Rico.
- Allstadt, K. E., Thompson, E. M., Bayouth García, D., Irizarry Brugman, E., Hernandez, J. L., Schmitt, R. G., et al. (2020). Field observations of ground failure triggered by the 2020 Puerto Rico earthquake sequence: U.S. *Geological Survey data release*. <https://doi.org/10.5066/P96QNFMB>
- Andrews, B. D., ten Brink, U. S., Danforth, W. W., Chaytor, J. D., Granja-Bruna, J.-L., Llanes Estrada, P., & Carbo-Gorosobel, A. (2014). Bathymetric terrain model of the Puerto Rico Trench and Northeast Caribbean for marine geological investigations. USGS OFR 2013-1125.
- Baldwin, W. E., Chaytor, J. D., Foster, D. S., Moore, E. M., Nichols, A. R., & ten Brink, U. S. (2021). *Multichannel seismic-reflection and navigation data collected using SIG ELC1200 and Applied Acoustics Delta Sparkers and Geometrics GeoEel Digital Streamers during U.S.*

at no cost. The authors thank Prof. Ernesto Otero, director, and Aldo Acosta, communication specialist, and Captain Orlando Espinoza and his crew for their generous help. Christa von Hillebrandt and Victor Huérfano helped facilitate logistical issues. This work contains modified Copernicus data from the Sentinel-1A and -1B satellites provided by the ESA. Original ALOS-2 data and products are copyright JAXA and provided under JAXA ALOS Research Announcement 6 (RA6). Part of this research was performed at the Jet Propulsion Laboratory, California Institute of Technology under contract with the National Aeronautics and Space Administration and supported by the Earth Surface and Interior focus area. The authors thank Robert Herrmann and Jessica Murray for helpful discussions and Kate Allstadt and Claudia Flores, USGS, for thorough and helpful reviews. Detailed and thoughtful comments by Tectonics Associate Editor Laura Giambiagi and by John Weber and an anonymous reviewer helped improve the manuscript. Any use of trade, firm, or product names is for descriptive purposes only and does not imply endorsement by the U.S. Government.

- Geological Survey Field Activity 2020-014-FA, southwest of Puerto Rico, March 2020: U.S. Geological Survey data release.* <https://doi.org/10.5066/P96GY6TQ>
- Ballantine, D. L., Appeldoorn, R. S., Yoshioka, P., Weil, E., Armstrong, R., Garcia, J. R., & Lilyestrom, C. (2008). Biology and ecology of Puerto Rican coral reefs. In *Coral reefs of the USA* (pp. 375–406). Dordrecht: Springer.
- Blewitt, G., Hammond, W. C., & Kreemer, C. (2018). Harnessing the GPS data explosion for interdisciplinary science. *Eos*, 99. <https://doi.org/10.1029/2018EO104623>
- Chaytor, J. D., & ten Brink, U. S. (2010). Extension in Mona Passage, Northeast Caribbean. *Tectonophysics*, 493, 74–92.
- Dascher-Cousineau, K., Lay, T., & Brodsky, E. E. (2020). Two foreshock sequences post Gulia and Wiemer (2019). *Seismological Society of America*, 91, 2843–2850.
- DeMets, C., Jansma, P. E., Mattioli, G. S., Dixon, T. H., Farina, F., Bilham, R., et al. (2000). GPS geodetic constraints on Caribbean-North America plate motion. *Geophysical Research Letters*, 27, 437–440.
- Fielding, E. J., Sangha, S. S., Bekaert, D. P. S., Samsonov, S. V., & Chang, J. C. (2017). Surface deformation of North-Central Oklahoma related to the 2016 Mw5.8 Pawnee Earthquake from SAR interferometry time series. *Seismological Research Letters*, 88, 971–982.
- Fielding, E. J., Vanacore, E., & López-Venegas, A. (2020). SAR imaging of the coseismic and postseismic deformation from the 2020 southwest Puerto Rico seismic sequence. *Geological Society of America Annual Meeting 2020*, presentation 139-4.
- Garrison, L. E. (1969). Structural geology of the Muertos insular shelf. *Puerto Rico US Geological Survey OFR*, 69–103.
- Geist, E. L., & ten Brink, U. S. (2021). Earthquake magnitude distributions on Northern Caribbean faults from combinatorial optimization models. *Journal of Geophysical Research*, 126, e2021JB022050. <https://doi.org/10.1029/2021JB022050>
- Graindorge, D., Klingelhoefer, F., Sibuet, J. C., McNeill, L., Henstock, T. J., Dean, S., & Shankar, U. (2008). Impact of lower plate structure on upper plate deformation at the NW Sumatran convergent margin from seafloor morphology. *Earth and Planetary Science Letters*, 275, 201–210.
- Granja-Bruña, J. L., ten Brink, U. S., Carbó-Gorosabel, A., Muñoz-Martín, A., & Gómez Ballesteros, M. (2009). Morphotectonics of central Muertos thrust belt and Muertos Trough (northeastern Caribbean). *Marine Geology*, 263, 7–33. <https://doi.org/10.1016/j.margeo.2009.03.010>
- Grindlay, N. R., Abrams, L. J., Del Greco, L., & Mann, P. (2005). Toward an integrated understanding of Holocene fault activity in Western Puerto Rico: Constraints from high-resolution seismic and side scan sonar data. Active tectonics and seismic hazards of Puerto Rico, the Virgin Islands, and offshore areas. *Geological Society of America Special Papers*, 385, 139–160.
- Grossman, I. G. (1963). Geology of the Guanica-Guayanilla Bay area, southwestern Puerto Rico. *U.S. Geological Survey Professional Paper*, 475-B, B114–B116.
- Harding, T. P. (1985). Seismic characteristics and identification of negative flower structures, positive flower structures, and positive structural inversion. *AAPG Bulletin*, 69, 582–600.
- Izart, A., Kemal, B. M., & Malod, J. A. (1994). Seismic stratigraphy and subsidence evolution of the northwest Sumatra fore-arc basin. *Marine Geology*, 122, 109–124.
- Kaneko, Y., & Fialko, Y. (2011). Shallow slip deficit due to large strike-slip earthquakes in dynamic rupture simulations with elasto-plastic off-fault response. *Geophysical Journal International*, 186, 1389–1403.
- Kaye, C. A. (1957). Notes on the structural geology of Puerto Rico. *Bulletin of the Geological Society of America*, 68, 103–118.
- Liang, C., & Fielding, E. J. (2017). Measuring azimuth deformation with L-Band ALOS-2 ScanSAR interferometry. *IEEE Transactions on Geoscience and Remote Sensing*, 55, 2725–2738. <https://doi.org/10.1109/TGRS.2017.2653186>
- Liu, C., Lay, T., Wang, Z., Xiong, X. (2020). Rupture process of the January 7, 2020, MW6.4 Puerto Rico earthquake. *Geophysical Research Letters*, 47, e2020GL087718.
- López-Venegas, A. M., Vanacore, E., & Hughes, S. K. (2020). Puerto Rico's Winter 2019–2020 seismic sequence leaves the island on edge. *Tembler*. <https://doi.org/10.32858/temblor.064>
- López-Venegas, A. M., Vanacore, E., Hughes, S. K., Báez- Sánchez, G., & Hudgins, T. R. (2020). Response and initial scientific findings from the southwestern Puerto Rico Seismic Sequence" (2020). *Tembler*. <https://doi.org/10.32858/temblor.068>
- Manaker, D. M., Calais, E., Freed, A. M., Ali, S. T., Przybylski, P., Mattioli, G., et al. (2008). Interseismic plate coupling and strain partitioning in the northeastern Caribbean. *Geophysical Journal International*, 174, 889–903. <https://doi.org/10.1111/j.1365-246X.2008.03819.x>
- Mann, P., Calais, E., Ruegg, J.-C., DeMets, C., & Jansma, P. E. (2002). Oblique collision in the north-eastern Caribbean from GPS measurements and geological observations. *Tectonics*, 21, 7–1. <https://doi.org/10.1029/2001TC0011304>
- Mann, P., Hippolyte, J. C., Grindlay, N. R., & Abrams, L. J. (2005). Neotectonics of southern Puerto Rico and its offshore margin. Active tectonics and seismic hazards of Puerto Rico, the Virgin Islands, and offshore areas. *Geological Society of America Special Papers*, 385, 173–214.
- Marshall, J. S., Fisher, D. M., & Gardner, T. W. (2000). Central Costa Rica deformed belt: Kinematics of diffuse faulting across the western Panama block. *Tectonics*, 19, 468–492.
- McCaffrey, R., Zwick, P. C., Bock, Y., Prawirodirdjo, L., Genrich, J. F., Stevens, C. W., & Subarya, C. (2000). Strain partitioning during oblique plate convergence in northern Sumatra: Geodetic and seismologic constraints and numerical modeling. *Journal of Geophysical Research*, 105, 28363–28376.
- Miranda, E., Acosta Vera, A., Aponte, L., Archbold, J., Cortes, M., Du, A., et al. (2020). StEER Puerto Rico M6.4 earthquake January 7, 2020 preliminary virtual reconnaissance report (PVRR), NHERI DesignSafe Project ID: PRJ-2670, Released: January 10, 2020.
- Monroe, W. H. (1980). Geology of the middle Tertiary formations of Puerto Rico, U.S. Geological Survey Professional Paper 953.
- Morales-Velez, A. C., Bernal, J., Hughes, K. S., Pando, M., Perez, J. C., Rodriguez, L. A., & Suarez, L. E. (2020). Geotechnical Reconnaissance of the January 7, 2020 M6.4 Southwest Puerto Rico Earthquake and Associated Seismic Sequence, Geotechnical Extreme Event Reconnaissance Report (GEER)-066. June 26, 2020.
- Pérez-Valentín, K., Barreto-Orta, M., Castro, A., Montañez-Acuña, A., & Cabrera-Valentín, N. (2021). Revealing geomorphic changes after the occurrence of a seismic event on the south coast of Puerto Rico (2020). *Shore and Beach*, 89, 22–33.
- Piety, L. A., Redwine, J. R., Derouin, S. A., Prentice, C. S., Kelson, K. I., Klinger, R. E., & Mahan, S. (2018). *Holocene surface ruptures on the Salinas fault and southeastern Great Southern Puerto Rico Fault Zone, South Coastal Plain of Puerto Rico* (Vol. 108, pp. 619–638). Bulletin of the Seismological Society of America. <https://doi.org/10.1785/0120170182>
- Pindell, J. L., & Kennan, L. (2009). Tectonic evolution of the Gulf of Mexico, Caribbean and northern South America in the mantle reference frame: An update. *Geological Society, London, Special Publications*, 328, 1–55.
- Prentice, C. S., & Mann, P. (2005). Paleoseismic study of the South Lajas fault: First documentation of an onshore Holocene fault in Puerto Rico. *Geological Society of America Special Paper*, 385, 215–222.
- Renken, R. A., Black, B. A., Ward, W. C., Gill, I. P., Gómez-Gómez, F., & Rodríguez-Martínez, J. (2002). Geology and hydrogeology of the Caribbean islands aquifer system of the commonwealth of Puerto Rico and the US Virgin Islands. US Geological Survey Prof. Pap. 1419.

- Roig-Silva, C. M., Asencio, E., & Joyce, J. (2013). The northwest-trending north Boquerón Bay-Punta Montalva fault zone—A through going active fault system in southwestern Puerto Rico. *Seismological Research Letters*, *84*, 538–550.
- Rosen, P. A., Gurrola, E., Sacco, G. F., & Zebker, H. (2012). The InSAR scientific computing environment. *Paper presented at 9th European Conference on Synthetic Aperture Radar, Nuremberg, Germany* (pp. 23–26).
- Ross, Z. E., Idini, B., Jia, Z., Stephenson, O. L., Zhong, M., Wang, X., & Jung, J. (2019). Hierarchical interlocked orthogonal faulting in the 2019 Ridgecrest earthquake sequence. *Science*, *366*, 346–351.
- Shcherbakov, R., & Turcotte, D. L. (2004). A modified form of Bath's law. *Bulletin of the Seismological Society of America*, *94*, 1968–1975.
- Solares-Colón, M. M. (2019). *New constraints on crustal deformation within the Puerto Rico-Virgin Islands microplate using two decades of GPS data* (M.Sc. thesis). University of Puerto Rico, Mayaguez.
- Symithe, S., Calais, E., de Chabaliér, J. B., Robertson, R., & Higgins, M. (2015). Current block motions and strain accumulation on active faults in the Caribbean. *Journal of Geophysical Research: Solid Earth*, *120*, 3748–3774. <https://doi.org/10.1002/2014JB011779>
- ten Brink, U. S. (2005). Vertical motions in the Puerto Rico trench and Puerto Rico and their cause. *Journal of Geophysical Research: Solid Earth*, *110*, B06404. <https://doi.org/10.1020/2004JB003459>
- ten Brink, U. S., Bakun, W. H., & Flores, C. H. (2011). Historical perspective on seismic hazard to Hispaniola and the NE Caribbean. *Journal of Geophysical Research: Solid Earth*, *116*, B12318. <https://doi.org/10.1029/2011JB008497>
- ten Brink, U. S., & López-Venegas, A. M. (2012). Plate interaction in the NE Caribbean subduction zone from continuous GPS observations. *Geophysical Research Letters*, *39*, L10304. <https://doi.org/10.1029/2012GL051485>
- ten Brink, U. S., Marshak, S., & Granja Bruña, J.-L. (2009). Bivergent thrust wedges surrounding oceanic island arcs: Insight from observations and sandbox models of the northeastern Caribbean plate. *The Geological Society of America Bulletin*, *121*, 1522–1536. <https://doi.org/10.1130/B26512.1>
- Toda, S., Stein, R. S., Sevilgen, V., & Lin, J. (2011). Coulomb 3.3 Graphic-rich deformation and stress-change software for earthquake, tectonic, and volcano research and teaching—user guide: U.S. Geological Survey Open-File Report 2011–1060, 63 p.
- Trumbull, J. V., & Garrison, L. E. (1973). Geology of a system of submarine canyons south of Puerto Rico. *Journal of Research of the U. S. Geological Survey*, *1*, 293–299.
- Vanacore, E. A., Joyce, J., ten Brink, U., Fielding, E. J., & López-Venegas, A. (2021). Double difference relocations of the southwestern Puerto Rico seismic sequence. *Seismological Research Letters*, *92*, 1444.
- von Hillebrandt-Andrade, C. G., López-Venegas, A., & Vanacore, E. (2020). 2019–2020 southwestern Puerto Rico Seismic Sequence. *TsunInfo Alert*, *22*, no. 1.
- Waldhauser, F., & Ellsworth, W. L. (2000). A double-difference earthquake location algorithm: Method and application to the northern Hayward fault, California. *Bulletin of the Seismological Society of America*, *90*(6), 1353–1368.
- Wells, D. L., & Coppersmith, K. J. (1994). New empirical relationships among magnitude, rupture width, rupture area, and surface displacement. *Seismological Society of America*, *84*, 974–1002.
- Withjack, M. O., Islam, Q. T., & La Pointe, P. R. (1995). Normal faults and their hanging-wall deformation: An experimental study. *AAPG Bulletin*, *79*, 1–17.
- Wright, T. J., Parsons, B. E., & Lu, Z. (2004). Toward mapping surface deformation in three dimensions using InSAR. *Geophysical Research Letters*, *31*, L01607.
- Yunjun, Z., Fattahi, H., & Amelung, F. (2019). Small baseline InSAR time series analysis: Unwrapping error correction and noise reduction. *Computers & Geosciences*, *133*, 104331. <https://doi.org/10.1016/j.cageo.2019.104331>